Optical Engineering

OpticalEngineering.SPIEDigitalLibrary.org

Multidiameter optical ring and Hermite–Gaussian vortices for wavelength division multiplexing–mode division multiplexing

Angela Amphawan
Yousef Fazea

SPIE.

Angela Amphawan, Yousef Fazea, "Multidiameter optical ring and Hermite–Gaussian vortices for wavelength division multiplexing–mode division multiplexing," *Opt. Eng.* **55**(10), 106109 (2016), doi: 10.1117/1.OE.55.10.106109.

Multidiameter optical ring and Hermite–Gaussian vortices for wavelength division multiplexing–mode division multiplexing

Angela Amphawan[a,b,*] and Yousef Fazea[a]
[a]Universiti Utara Malaysia, School of Computing, Optical Computing and Technology Research Laboratory, Sintok, Kedah 06010, Malaysia
[b]Massachusetts Institute of Technology, Research Laboratory of Electronics, Cambridge, Massachusetts 02319, United States

Abstract. Optical vortices are high-capacity data carriers for mode division multiplexing (MDM) in multimode fiber (MMF). This paper reports on the MDM of a combination of helical-phased optical vortices comprising donut modes and Hermite–Gaussian (HG) modes for different radial offsets from the MMF axis. A data rate of 44 Gbps is achieved for wavelength division multiplexing–MDM of two pairs of helical-phased donut mode and HG mode at wavelengths 1550.12 and 1551.72 nm for a MMF length of 1500 m. © *2016 Society of Photo-Optical Instrumentation Engineers (SPIE)* [DOI: 10.1117/1.OE.55.10.106109]

Keywords: donut mode; Hermite–Gaussian mode; mode division multiplexing; wavelength division multiplexing.
Paper 160061 received Jan. 13, 2016; accepted for publication Aug. 5, 2016; published online Oct. 13, 2016.

1 Introduction

Rigorous developments have demonstrated that optical vortices with helical phase fronts may be harnessed for a diversity of emerging applications, recently extended to optical communications, particularly for mode division multiplexing (MDM). In MDM, each fiber mode in a multimode fiber (MMF) is treated as a separate channel that is capable of carrying its own data independently using fiber eigenmodes. In light of the fundamental capacity limit governed by fiber nonlinearity,[1] MDM is an evolutionary approach for increasing the possible degrees of freedom for exponential bandwidth growth, in conjunction with other multiplexing schemes based on intensity, wavelength, time, code, and polarization.[2–4]

MDM has spurred innovative techniques for generating various optical vortices for compensating for degenerate mode group (DMG) dispersion and mode coupling, which restrict the coherence length of DMGs in few-mode fiber and MMF.[5–11] Spatial light modulators (SLMs) have been used for holographic shaping of the wavefront to different linearly polarized modes or orbital angular momentum (OAM) modes externally[12–15] or within the laser cavity.[16,17] A coherent superposition of optical vortex modes can be used to create multimoded signals. In Ref. 18, a spiral-phased plate (SPP) resonator is used to generate a coherent superposition of optical vortices with different winding numbers. The SPP transmission function is calculated from the low-reflectivity to high-reflectivity regime. The superposition of coherent optical vortices after multiple reflections is investigated by varying the surface reflection coefficient and the propagation distances in Ref. 19, and the wave transfer matrix is applied to the SPP to calculate the effect of a substrate with different refractive indices from the SPP on the rotation dynamics of the optical vortex.[20] In Ref. 21, microscale spiral phase plates were inserted into the aperture of a vertical-cavity surface-emitting laser (VCSEL) to convert the linearly polarized Gaussian beam emitted into a beam carrying specific OAM modes and their superposition states. In Ref. 22, Laguerre–Hermite–Gaussian modes from confocal resonator eigen-functions of the Fraunhofer diffraction integral are introduced. For multimoded signal propagation, photonic crystal fibers with different combinations of trench-assisted[23,24] and hole-assisted[25] refractive index profiles have been realized with low crosstalk between generated linearly polarized modes[26] and OAM modes.[27] In addition, photonic lanterns from several single mode fibers in a low refractive index capillary tube, which are adiabatically tapered, have demonstrated efficient coupling into different linearly polarized modes.[28,29] Another approach for MDM is to fabricate nonconcentric multiring fiber switch with significant difference in effective refractive index of fiber eigenmodes between cores to mitigate intermodal crosstalk between OAM modes.[30] To improve spatial channel densities, multielement fiber (MEF) comprising multiple fiber elements that are drawn and coated together in a common polymer coating has been fabricated.[31] To decouple the channels at the receiver, several methods for estimation of the channel matrix and adaptive equalization have been postulated.[32–35]

Although laudable goals have been forged in experimental demonstration of MDM adopting nonconcentric rings either by multicore fibers or MEFs, these new class of optical fibers still require a compatible multimoded laser source. For OAM modes with varying diameters, to extend the work in Refs. 16, 17, and 21 based on intracavity SLMs, a VCSEL with an intracavity SLM generating concentric multidiameter optical ring vortices and HG vortices is proposed. In this paper, for the first time, MDM of concentric multidiameter optical ring vortices and HG vortices from an intracavity VCSEL is numerically simulated.

*Address all correspondence to: Angela Amphawan, E-mail: angela.amphawan.dr@ieee.org

This paper is organized as follows. Section 1 provides a brief overview of related research in MDM. Section 2 reports on the new MDM model for helical-phased donut modes and radially offset HG modes. Section 3 analyzes the power-coupling coefficients, DMG delays, and bit error rates (BER) for different radial offsets. The paper is concluded in Sec. 4.

2 Methodology

The MDM of four spiral-phased donut modes in MMF was modeled in Optsim 5.2[36] and MATLAB,[37] as shown in Fig. 1.

The transmitter constitutes two VCSEL arrays on wavelengths of 1550.12 and 1551.72 nm, each exciting two x-polarized donut modes of different diameters and HG modes. The VCSEL draws the electrical current injected into the cavity and solves for the optical output using spatially independent rate equations[38]

$$\frac{dN_0}{dt} = \frac{\eta_i I}{q} - \frac{N_0}{\tau_n} - \frac{G(T)\{\gamma_{00}[N_0 - N_t(T)] - \gamma_{01}N_1\}}{1+\varepsilon S} S - \frac{I_1(N_0,T)}{q}, \tag{1}$$

$$\frac{dN_1}{dt} = -\frac{N_1}{\tau_n}(1+h_{\text{diff}}) + \frac{G(T)\{\phi_{100}[N_0 - N_t(T)] - \phi_{101}N_1\}}{1+\varepsilon S} S, \tag{2}$$

$$\frac{dS}{dt} = -\frac{S}{\tau_p} + \frac{\beta N_0}{\tau_n} + \frac{G(T)\{\gamma_{00}[N_0 - N_t(T)] - \gamma_{01}N_1\}}{1+\varepsilon S} S, \tag{3}$$

where N_0 is the average carrier number, N_1 is the spatial hole produced by the fundamental transverse mode, τ_n is the carrier lifetime, τ_p is the photon lifetime, q is the electron charge, V is the effective active-layer volume, I is the spatially dependent injection current, S is the total photon number, T is the device temperature, G is the gain, I_1 is the thermal leakage current, η_I is the current-injection efficiency, β is the spontaneous-emission coupling coefficient, and ε is the gain saturation factor. To represent the thermally dependent gain of the VCSEL, the gain constant, $G(T)$, and transparency number, $N_t(T)$, are described by[38]

$$G(T) = G_o \frac{a_{g0} + a_{g1}T + a_{g2}T^2}{b_{g0} + b_{g1}T + b_{g2}T^2}, \tag{4}$$

$$N_t(T) = N_{tr}(c_{n0} + c_{n1}T + c_{n2}T^2), \tag{5}$$

where G_o is the gain constant, a_{g0}, a_{g1}, a_{g2}, b_{g0}, b_{g1}, b_{g2}, c_{n0}, c_{n1}, and c_{n2} are used as fitting parameters. Thermally dependent carrier leakage is expressed as[39]

$$I_l(N_0,T) = I_{lo} \exp\left(\frac{-a_0 + a_1 N_0 + a_2 N_0 T - a_3/N_0}{T}\right), \tag{6}$$

where I_{lo} is the leakage current factor and a_0, a_1, a_2, and a_3 are used as fitting parameters. The output power is given by[38]

$$P_{\text{out}} = k_f S, \tag{7}$$

where k_f is the output-power-coupling coefficient and S is the total photon number. The time-derivative of the optical phase ϕ_o from the VCSEL, is modeled using[40]

$$\frac{d\phi_o}{dt} = \frac{\tau}{2} \cdot \frac{G(T)[\gamma_{00}(N_0 - N_{\text{th}}) - \gamma_{01}N_1]}{1+\varepsilon S}, \tag{8}$$

where τ is the linewidth enhancement factor and N_{th} is the room-temperature threshold. For a beam of wavelength λ at a distance z along the beam from the beam waist, the variation of the spot size, w is given by

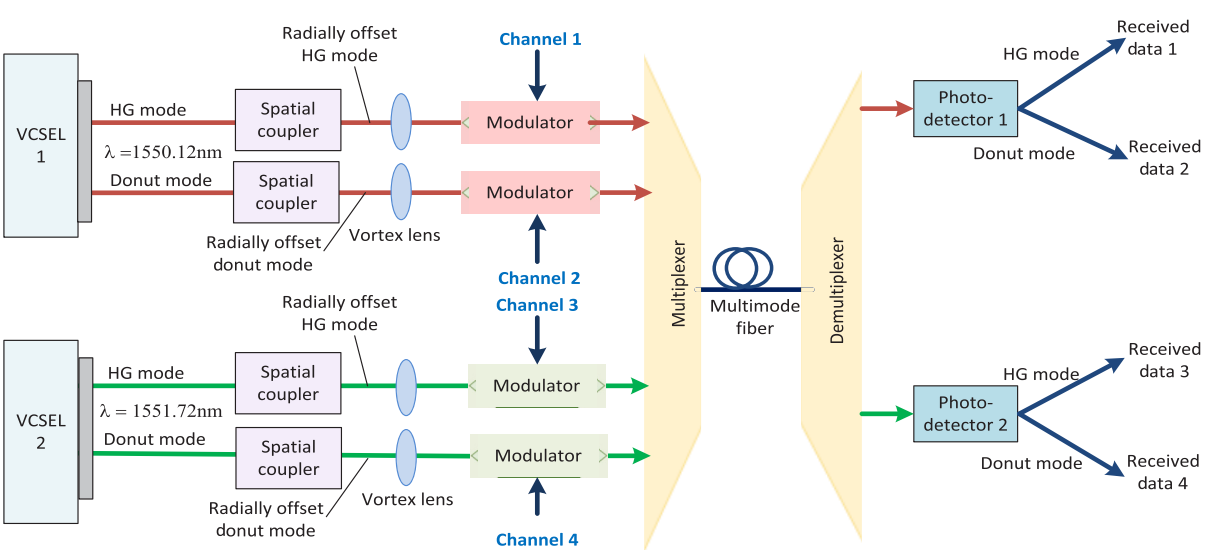

Fig. 1 MDM model for helical-phased donut modes and HG modes on two wavelengths.

$$w(z) = w_0[1 + (z/z_R)^2]^{\frac{1}{2}}. \quad (9)$$

A total of four channels were employed at both wavelengths 1550.12 nm on VCSEL 1 and 1551.72 nm on VCSEL 2. An intracavity SLM is employed to generate donut modes and HG modes on different channels as follows:

(a) Channel 1—VCSEL 1 emits an HG mode with x-index 0 and y-index 2.
(b) Channel 2—VCSEL 1 emits a donut mode with an outer diameter of 12 μm and an inner diameter of 10 μm.
(c) Channel 3—VCSEL 2 emits an HG mode with x-index 0 and y-index 2.
(d) Channel 4—VCSEL 2 emits a donut mode with an outer radius of 15 μm, and an inner radius of 13 μm.

The HG modes from the two VCSELs are radially offset from the MMF axis by a specified value, b, ranging from 1 to 4 μm. The magnitude and phase distributions of transverse electric field of helical-phased donut and $HG_{2,0}$ mode from VCSEL array are shown in Fig. 2. The VCSEL is driven by independent pseudorandom binary sequence electrical signals and optically modulated to nonreturn-to-zero pulses.

The transverse electric field of the HG mode is defined as[36]

$$\psi_{\mathrm{HG}\,u,v}(x,y) = \sigma \cdot H_u\left(\frac{\sqrt{2}x}{w_{0y}}\right) \cdot \exp\left(\frac{-x^2}{w_{0x}^2}\right) \cdot \exp\left(\frac{j\pi x^2}{\lambda R_{0x}}\right) \cdot H_v\left(\frac{\sqrt{2}y}{w_{0y}}\right) \cdot \exp\left(\frac{-y^2}{w_{0y}^2}\right) \cdot \exp\left(\frac{j\pi y^2}{\lambda R_{0y}}\right), \quad (10)$$

where u and v are the x-index and y-index of the H_u and H_v Hermite polynomials in the x-axis and y-axis directions, respectively, σ is the scaling constant used to normalize the transverse electric field to a maximum value of 1, w_{0x} and w_{0y} are the spot sizes in the x-axis and y-axis, respectively; R_{0x} and R_{0y} are the x and y radii of curvature, respectively; the x and y differences in field profile are subjective to the polynomial factors for the order numbers u and v.

The transverse electrical field profile of the donut mode from the VCSEL is described as[36]

$$\psi_d(x,y) = \begin{cases} \kappa, & r_{\min} \le r \le r_{\max} \\ 0, & r < r_{\min}, r > r_{\max} \end{cases}, \quad (11)$$

where κ is normalization constant, $r_{\min}$ is the minimum radius, and $r_{\max}$ is the maximum radius of the donut. Within the minimum and maximum radii, the electric field is constant, whereas outside of these bounds, the transverse electric field is zero.

Each VCSEL is connected to a vortex lens used to add a helical phase front to the HG modes and donut modes. The applied phase transformation is expressed as[36]

$$t(x,y) = \exp\left[-j\left(\frac{n\pi r^2}{2\lambda f} + p\theta\right)\right], \quad (12)$$

$$r = x^2 + y^2, \quad (13)$$

$$\theta = \tan^{-1}(y/x), \quad (14)$$

where x and y are the transverse coordinates of the electric field in the $x-y$ plane, λ is the signal wavelength, $p = 2$ is the vortex order of the vortex lens, $n = 1.4$ is the material refractive index, and $f = 8.0$ mm is the lens focal length.

The MDM signals are then propagated through a 1500-m long MMF with a refractive index profile described by[41]

$$n(R) = n_{\mathrm{co}}(1 - \Delta R^{\alpha}), \quad (15)$$

where n_{co} is the maximum refractive index of the core, R is the normalized radial distance from the center of the core, $\Delta = (n_{\mathrm{co}}^2 - n_{\mathrm{cl}}^2)/(2n_{\mathrm{co}}^2)$ is the profile height parameter, n_{cl} is the refractive index of the cladding at $R = 1$, and α is the refractive index profile parameter. For a parabolic refractive index profile, $\alpha = 2$ whereas manufactured MMF have α values between 1.8 and 2.2. In this work, $\alpha = 1.9$ was used.

The total output electric field from the spiral-phased HG modes and donut modes may be described as

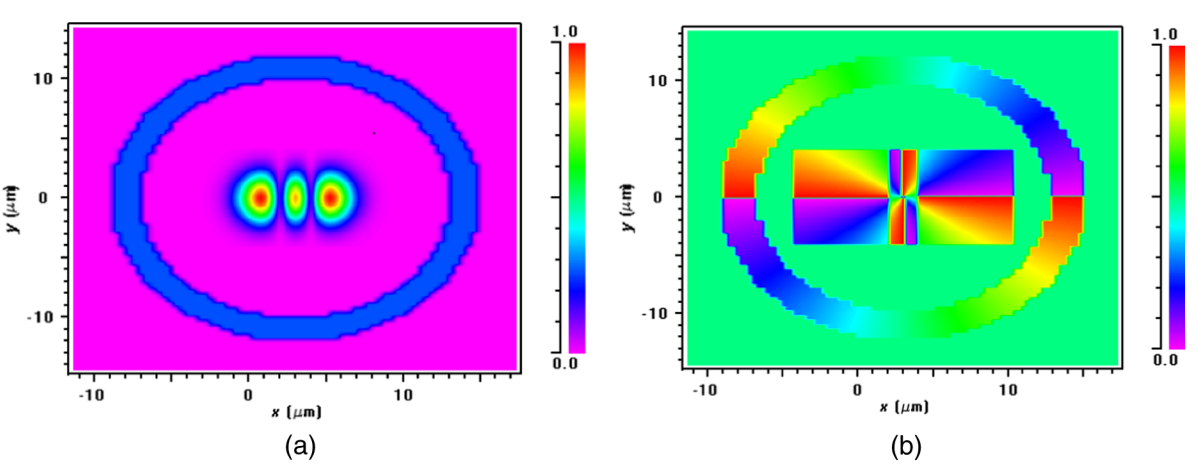

Fig. 2 (a) Magnitude and (b) phase distributions of transverse electric field of helical-phased donut and $HG_{2,0}$ mode from VCSEL array.

$$E_{\text{out}}(r,\phi,t)=\sum_{l}\sum_{m}c_{lm}e_{lm}(t-\tau_{lm})E^{i}_{lm}(r,\phi)\exp(j\beta_{lm}z). \tag{16}$$

Each mode experiences a different time delay[42]

$$\tau_q = L\frac{\mathrm{d}\beta_q}{\mathrm{d}\omega}, \tag{17}$$

where L is the length and ω is the optical angular frequency.

Each fiber mode experiences different mode attenuation, accounted by[43]

$$\gamma=\gamma_0\left(1+I_p\left\{\eta\left[\frac{(|l|+2m)\lambda}{2\pi\rho n_{\text{co}}}\sqrt{\frac{\alpha+2}{\alpha\Delta}}\right]^{\frac{2\alpha}{\alpha+2}}\right\}\right), \tag{18}$$

where γ_0 is the basic attenuation seen by all modes, I_p is the pth order modified Bessel function of the first kind, η is a scaling factor, n_{co} is the maximum core refractive index, ρ is the core radius, Δ is the profile height parameter, α is the profile alpha parameter of the refractive index. Chromatic dispersion is described by

$$D(\lambda)=\frac{S_0\lambda}{4}\left(1-\frac{\lambda_0^4}{\lambda^4}\right), \tag{19}$$

where λ is the operating wavelength of interest, λ_0 is the zero dispersion wavelength, and S_o is the dispersion slope at λ_0. Power modal coupling, caused by microbending and perturbations of the optical fiber cross section, is assumed to lead to nearest-neighbor coupling and solved iteratively using[44]

$$\frac{\partial P_q}{\partial z}+\tau_q\frac{\partial P_q}{\partial t}=-\alpha_q P_q+\kappa_q d_q(P_{q+1}-P_q)-\gamma_{q-1}d_{q-1}(P_q-P_{q-1}), \tag{20}$$

where q is the mode group number, which varies between 1 and $q_{\max}$, $P_q(z,t)$ is the average power signal for mode group q, v_q is the mode group velocity, α_q is the power attenuation coefficient for mode group q, and κ_q and γ_q are the degeneracy factors for the number of modes exchanging power between mode groups q and $q+1$, d_q is the mode-coupling coefficient between mode groups q and $q+1$ governed by

$$d_q=\frac{1}{8}\left(\frac{2\pi n_{\text{co}}\rho}{\lambda}\right)\left(\frac{q}{q_{\max}}\right)^{\frac{4}{\alpha+2}}\frac{C_o}{\Delta\beta_q^{2p}}, \tag{21}$$

where C_o is a mode-coupling factor, p is the phenomenological parameter with the values of 0, 1 or 2, $\Delta\beta_q$ is the difference in average propagation constants between mode groups $q+1$ and q.

The power-coupling coefficient between the output field of each VCSEL array and each transverse modal field of the MMF is calculated as follows:[45]

$$c_{lm}=\int_0^{2\pi}\int_0^{\infty}E^{i}_{lm}(r,\phi)\cdot e^{*}_{lm}(r,\phi)\cdot r\mathrm{d}r\,\mathrm{d}\phi, \tag{22}$$

where $E^{i}_{lm}(r,\phi)$ is the incident electric field from each individual element of the VCSEL array on the MMF and e_{lm} is the transverse electric field of linearly polarized modes of an infinite parabolic MMF obtained by solving the Helmholtz scalar wave equation and results in a superposition of the function Ψ given by[46]

$$\Psi=\begin{cases}F\cos(l\phi)\\ F\sin(l\phi)\end{cases}, \tag{23}$$

where the radial wave-function F_l is described by[41]

$$F_l=R^l L^{(l)}_{m-1}(VR^2)\exp\left(-\frac{VR^2}{2}\right), \tag{24}$$

where $L^{(l)}_{m-1}$ is the generalized Laguerre polynomial,[47] V is the normalized frequency, given by $V=(2\pi\text{NA}\rho)/\lambda$, where NA is the numerical aperture of the particular MMF and λ is the free-space wavelength of the incident optical source into the fiber. The signals are then retrieved at four photodetectors at wavelengths 1550.12 and 1551.72 nm. The modes are retrieved based on noninterferometric modal decomposition. The results and analysis are presented in Sec. 3.

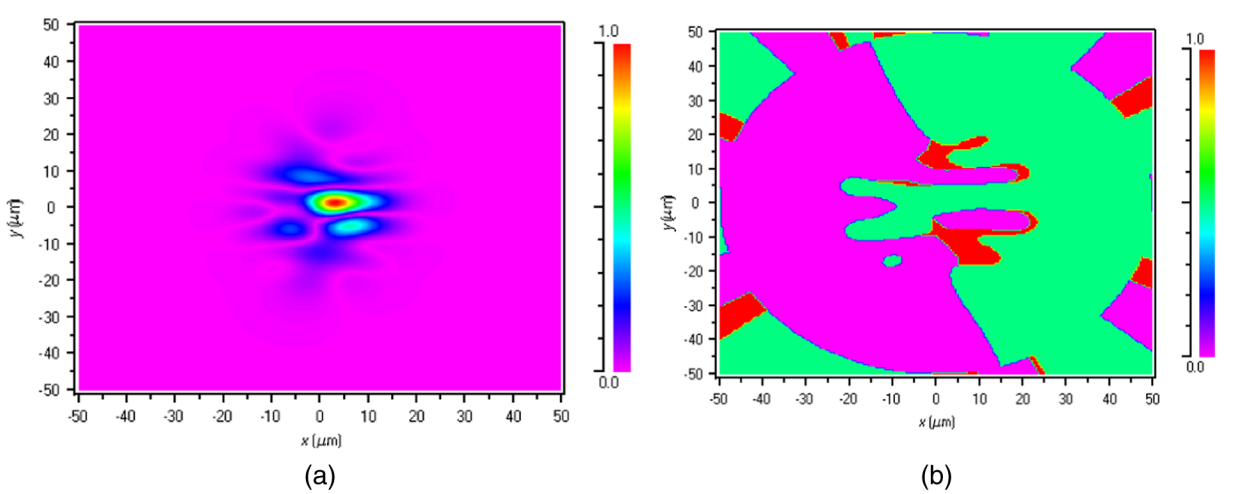

Fig. 3 (a) Magnitude and (b) phase distribution of transverse electric field after propagating through MMF for radial offset, $b=3$ μm from MMF axis and vortex order, $p=2$ for channel 2.

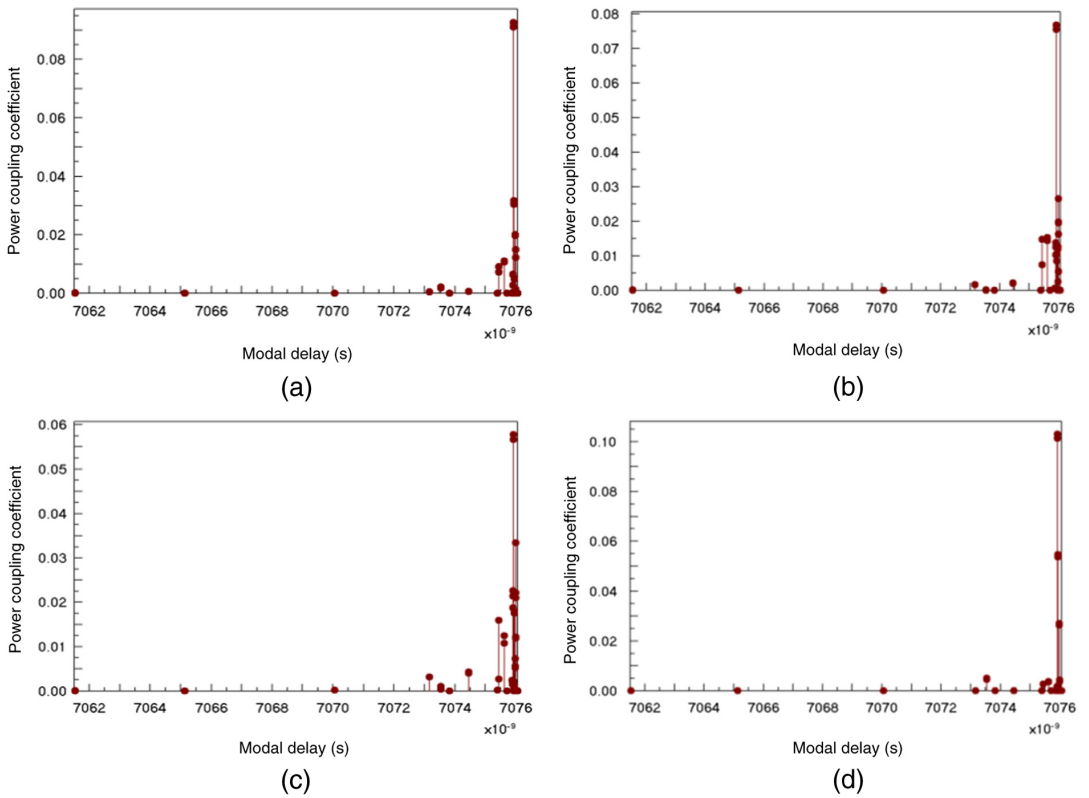

Fig. 4 Power coupling coefficient versus modal delay at the MMF output for wavelength 1550.12 nm for a radial offset of b: (a) $b = 1$ μm, (b) $b = 2$ μm, (c) $b = 3$ μm, and (d) $b = 4$ μm.

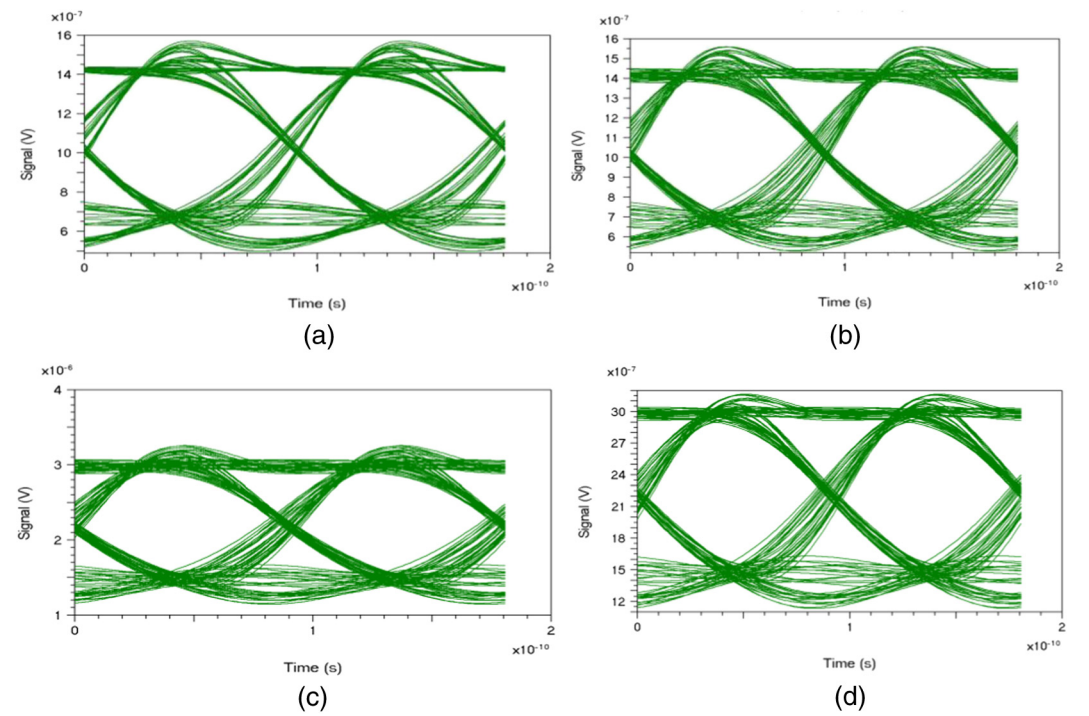

Fig. 5 Eye diagrams for different radial offsets with respect to MMF axis, b: (a) $b = 1$ μm, (b) $b = 2$ μm, (c) $b = 3$ μm, and (d) $b = 4$ μm for a distance of 1500 m at wavelength 1550.12 nm.

3 Results and Discussions

A qualitative evaluation of the effects of different radial offsets of the HG-ring vortices is made. Figure 3 shows an example of the output transverse electric field for mode HG_{20} after propagating through the MMF for Channel 2. As observed in Fig. 3, the intensity of the spatial field still can be determined after a distance of 1500 m.

For quantitative evaluation, the modal decomposition at the MMF output is analyzed for different radial offsets. Figure 4 shows the power-coupling coefficients versus modal delay for the HG_{20} after the modes propagate through the MMF at wavelength 1550.12 nm. In Figs. 4(a)–4(d), the power is coupled dominantly into higher-order modes while strong mode suppression has been observed in medium- and lower-order modes. Thus, the propagation delay between modes is reduced and the pulses are more distinct, as confirmed in Figs. 5(a)–5(d) from the eye diagrams.

In Fig. 6(a), the excited modes are more tightly clustered in higher-order modes and strong mode suppression is observed in lower-order modes. This results in a very clean eye at the output as observed in Fig. 7(a). From Figs. 6(b) to 6(d), the power is coupled into a wide range of medium-ranged modes and extreme lower-order modes, each of which arrives at the fiber output at different times. This results in a nearly undistinguished eye as confirmed by Figs. 7(b)–7(d).

Figure 8 shows the power-coupling coefficients in DMGs and the differential mode delay (DMD) of the DMGs at wavelength 1550.12 nm. From the curves, it is evident that acceptable DMD is achieved when the radial offset b, is varied at $b = 1$, $b = 2$, $b = 3$, and $b = 4$.

Figure 9 shows the power-coupling coefficients of DMGs and DMD of the DMGs at wavelength 1551.72 nm. From the curves, it is evident that the best DMD is achieved when the radial offset $b = 1$. Symmetric and antisymmetric modes are observed in the power-coupling coefficients of degenerate modes due to opposing propagation constants.

For a comparison at different radial offsets, the BERs were examined, as shown in Fig. 10. Figure 10 demonstrates reliable BER values for all radial offsets at 44 Gbit/s. In Fig. 10(a), the spiral-phased HG-ring MDM system at wavelength 1550.12 achieves the lowest BER for radial offset of 4 μm, followed by radial offset of 1 μm, radial offset 2 μm, and radial offset 3 μm. In Fig. 10(b), the spiral-phased HG-ring MDM system at wavelength 1551.72 achieves the lowest BER for radial offset of 1 μm, followed by radial offset of 2 μm, while radial offset 3 μm and radial offset 4 μm experience high BERs. This is consistent with the power-coupling coefficient of individual modes and DMDs obtained in previous figures.

The results imply that the new MDM scheme is tolerant to small misalignments of about 4 μm. The robustness of the

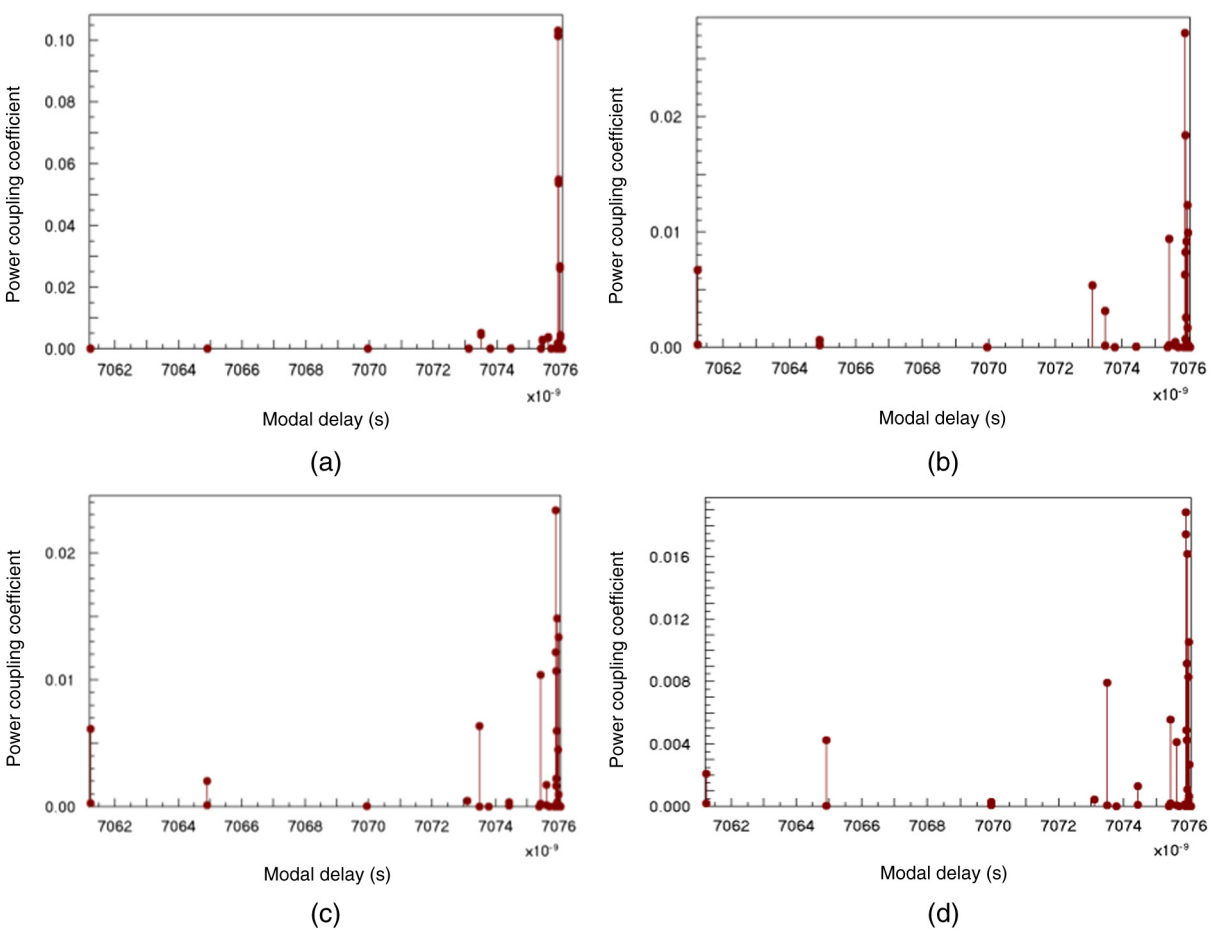

Fig. 6 Power coupling coefficient versus modal delay at the MMF output for wavelength 1550.12 nm for radial offset *b*: (a) $b = 1$ μm, (b) $b = 2$ μm, (c) $b = 3$ μm, and (d) $b = 4$ μm.

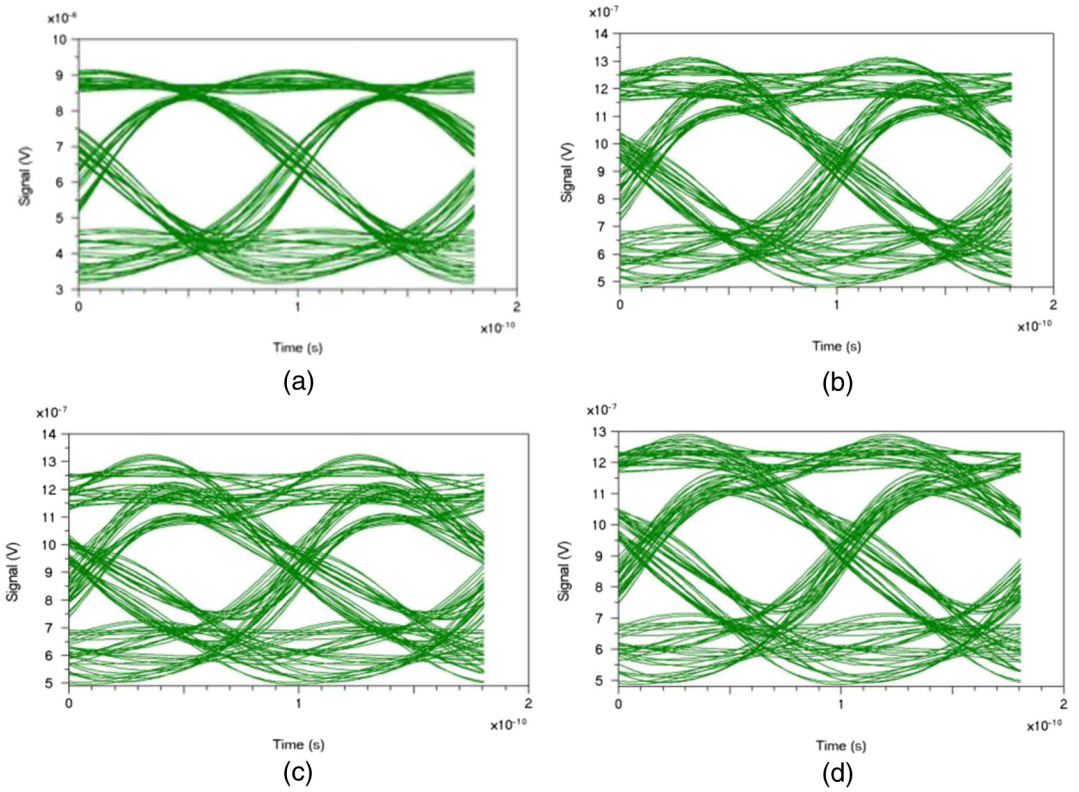

Fig. 7 Eye diagrams for different radial offsets with respect to MMF axis, b: (a) $b = 1$ μm, (b) $b = 2$ μm, (c) $b = 3$ μm, and (d) $b = 4$ μm for a distance of 1500 m at wavelength 1550.12 nm.

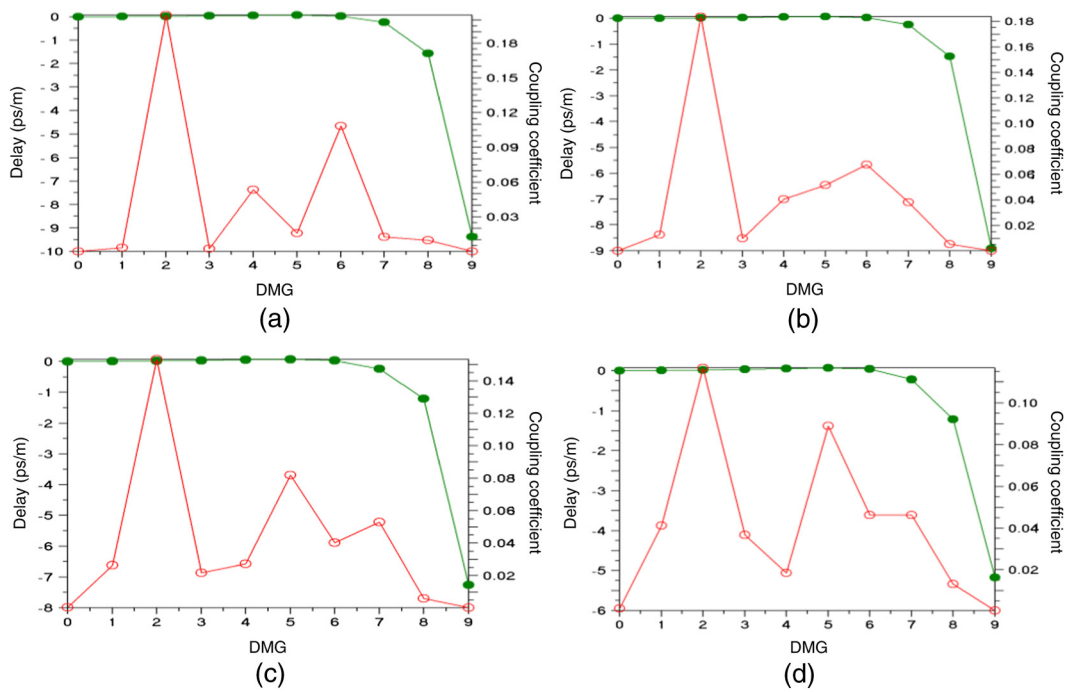

Fig. 8 Relative propagation delay versus DMG (green line and filled marker) and power-coupling coefficient versus DMG (red line and hollow marker) for wavelength 1550.12 nm for different radial offsets with respect to MMF axis, b: (a) $b = 1$ μm, (b) $b = 2$ μm, (c) $b = 3$ μm, and (d) $b = 4$ μm.

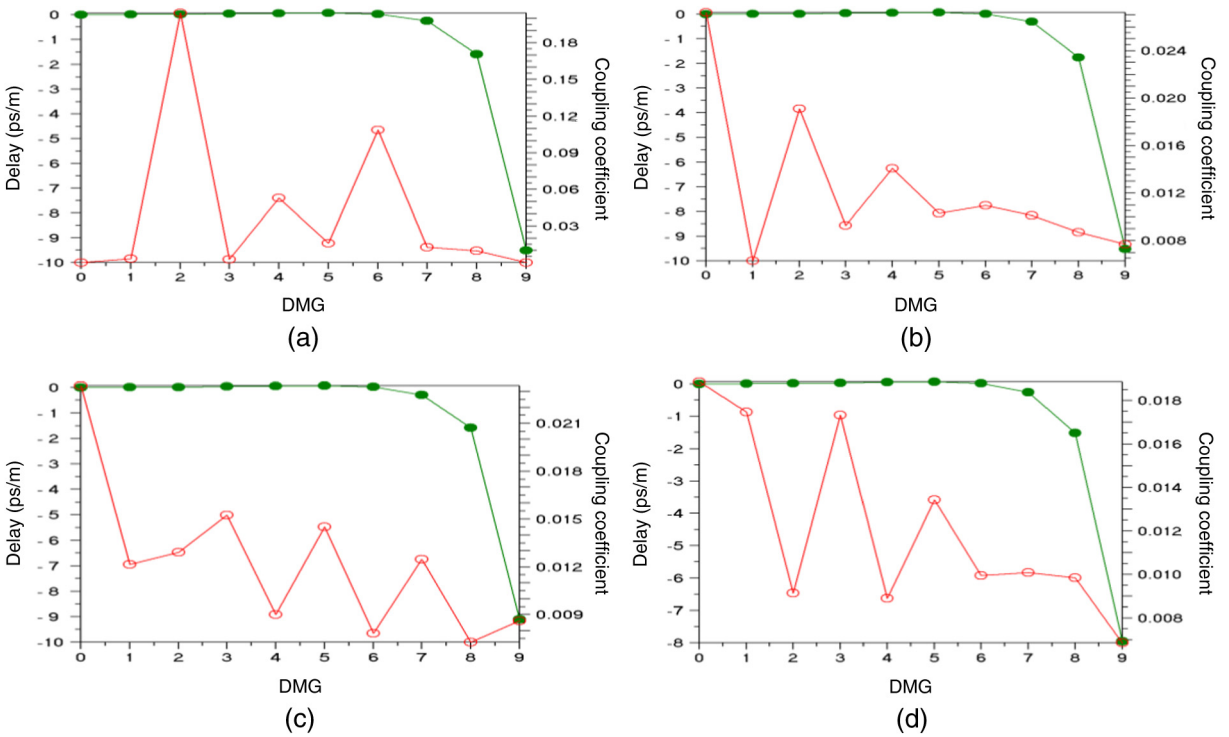

Fig. 9 Relative propagation delay versus DMG (green line and filled marker) and power-coupling coefficient versus DMG (red line and hollow marker) for wavelength 1551.72 nm for different radial offsets with respect to MMF axis, b: (a) $b = 1$ μm, (b) $b = 2$ μm, (c) $b = 3$ μm, and (d) $b = 4$ μm.

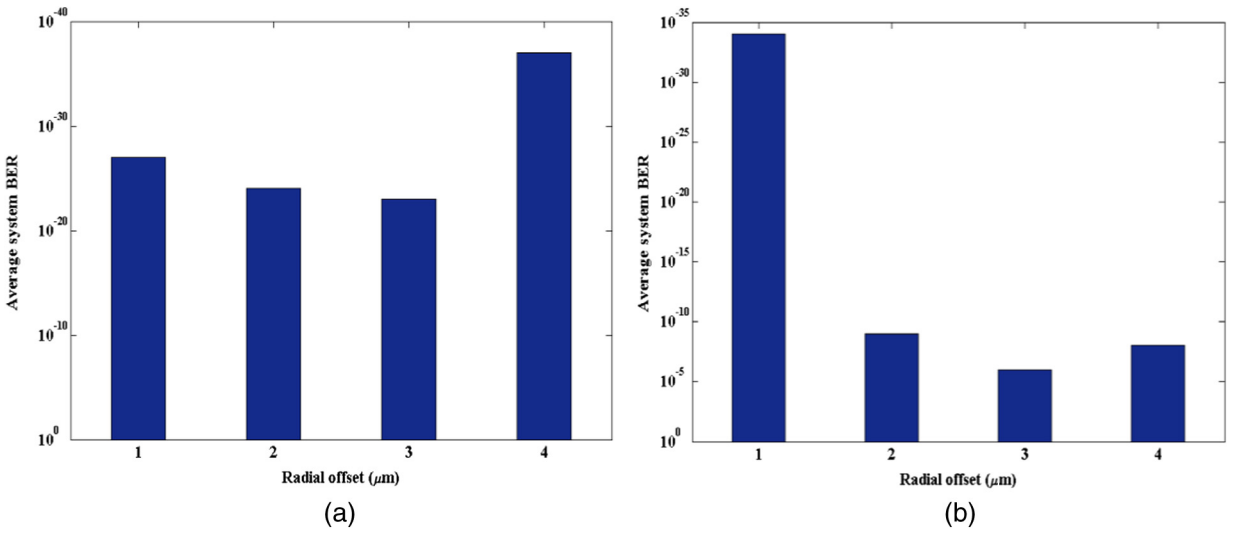

Fig. 10 Average BER for (a) wavelength 1550.12 nm and (b) wavelength 1551.72 nm for different radial offsets with respect to MMF axis.

HG-ring vortex MDM launch is evident from the low BER values at 44 Gbit/s and is significantly lower than BER values obtained from single-channel pure HG mode launches at a data rate of 10 Gbit/s.[48]

4 Conclusion

Data transmission of 44 Gbit/s is achieved for a 2×2 MDM–WDM model using two pairs of radially offset spiral-phased HG-ring vortices and ring vortices on wavelengths 1550.12 and 1551.72 nm, respectively. The spiral-phased HG-ring MDM launch is tolerant to small misalignments of up to 4 μm and achieves better BER performance at a higher data rate than pure HG mode launches. The model may find viable applications for optical interconnects and logical switches.

References

1. D. J. Richardson, J. M. Fini, and L. E. Nelson, "Space-division multiplexing in optical fibres," *Nat. Photonics* **7**(5), 354–362 (2013).
2. A. Amphawan, "Review of optical multiple-input–multiple-output techniques in multimode fiber," *Opt. Eng.* **50**, 102001 (2011).

3. A. Amphawan, Y. Fazea, and H. Ibrahim, "Investigation of channel spacing for Hermite–Gaussian mode division multiplexing in multimode fiber," in *11th IEEE Int. Colloquium on Signal Processing and its Applications (CSPA)*, pp. 34–39 (2015).
4. H. M. R. Al-Khafaji et al., "Reducing BER of spectral-amplitude coding optical code-division multiple-access systems by single photodiode detection technique," *J. Eur. Opt. Soc.* **8**, 1–5 (2013).
5. G. C. G. Berkhout et al., "Efficient sorting of orbital angular momentum states of light," *Phys. Rev. Lett.* **105**(15), 153601 (2010).
6. A. Amphawan et al., "Effect of vortex order on helical-phased donut mode launch in multimode fiber," *Adv. Sci. Lett.* **21**(10), 3042–3045 (2015).
7. Y. Fazea and A. Amphawan, "5 × 5 25 Gbit/s WDM-MDM," *J. Opt. Commun.* **36**, 327–333 (2015).
8. Y. Fazea, A. Amphawan, and A. Ahmad, "Spot mode excitation for multimode fiber," in *4th Int. Conf. on Internet Applications, Protocols and Services (NETAPPS2015)* (2015).
9. A. Amphawan, Y. Fazea, and M. Elshaikh, "Space division multiplexing in multimode fiber for channel diversity in data communications," in *Advanced Computer and Communications Engineering Technology*, A. H. Sulaiman et al., Eds., pp. 355–363, Springer, Switzerland (2016).
10. A. Amphawan and Y. Fazea, "Laguerre-Gaussian mode division multiplexing in multimode fiber using SLMs in VCSEL arrays," *J. Eur. Opt. Soc.-Rapid Publ.* **12**, 12 (2016).
11. A. Amphawan et al., "MDM of hybrid modes in multimode fiber," in *Electrical Engineering, Computer Science and Informatics (EECSI)* (2015).
12. R. Brüning et al., "Direct fiber excitation with a digitally controlled solid state laser source," *Opt. Lett.* **40**(3), 435–438 (2015).
13. J. Carpenter and T. D. Wilkinson, "All optical mode-multiplexing using holography and multimode fiber couplers," *J. Lightwave Technol.* **30**(12), 1978–1984 (2012).
14. A. Amphawan and D. O'Brien, "Holographic mode field generation for a multimode fiber channel," in *IEEE Int. Conf. on Photonics (ICP2010)*, pp. 1–5 (2010).
15. A. Amphawan, "Binary spatial amplitude modulation of continuous transverse modal electric field using a single lens for mode selectivity in multimode fiber," *J. Mod. Opt.* **59**(5), 460–469 (2012).
16. Y.-M. Jung et al., "Spatial mode switchable, wavelength tunable erbium doped fiber laser incorporating a spatial light modulator," in *OSA Technical Digest (Online), Optical Fiber Communication Conf.*, Tu3D.4 (2014).
17. S. Ngcobo et al., "A digital laser for on-demand laser modes," *Nat. Commun.* **4**, 2289 (2013).
18. Y. S. Rumala and A. E. Leanhardt, "Multiple-beam interference in a spiral phase plate," *J. Opt. Soc. Am. B* **30**(3), 615–621 (2013).
19. Y. S. Rumala, "Propagation of structured light beams after multiple reflections in a spiral phase plate," *Opt. Eng.* **54**(11), 111306 (2015).
20. Y. S. Rumala, "Wave transfer matrix for a spiral phase plate," *Appl. Opt.* **54**(14), 4395–4402 (2015).
21. H. Li et al., "Orbital angular momentum vertical-cavity surface-emitting lasers," *Optica* **2**(6), 547–552 (2015).
22. S. Cunzhi, J. Pu, and S. Chávez-Cerda, "Elegant Cartesian Laguerre–Hermite–Gaussian laser cavity modes," *Opt. Lett.* **40**(6), 1105–1108 (2015).
23. S. Li and J. Wang, "A compact trench-assisted multi-orbital-angular-momentum multi-ring fiber for ultrahigh-density space-division multiplexing (19 rings × 22 modes)," *Sci. Rep.* **4**, 3853 (2014).
24. A. Amphawan, B. Nedniyom, and N. M. Al Samman, "Selective excitation of LP01 mode in multimode fiber using solid-core photonic crystal fiber," *J. Mod. Opt.* **60**(20), 1675–1683 (2013).
25. R. G. H. van Uden et al., "Ultra-high-density spatial division multiplexing with a few-mode multicore fibre," *Nat. Photonics* **8**(11), 865–870 (2014).
26. T. Watanabe and Y. Kokubun, "Ultra-large number of transmission channels in space division multiplexing using few-mode multi-core fiber with optimized air-hole-assisted double-cladding structure," *Opt. Express* **22**(7), 8309–8319 (2014).
27. C. Brunet et al., "Design, fabrication and validation of an OAM fiber supporting 36 states," *Opt. Express* **22**(21), 26117–26127 (2014).
28. J. Carpenter et al., "1 × 11 few-mode fiber wavelength selective switch using photonic lanterns," *Opt. Exp.* **22**(3), 2216–2221 (2014).
29. B. Huang et al., "All-fiber mode-group-selective photonic lantern using graded-index multimode fibers," *Opt. Express* **23**(1), 224–234 (2015).
30. M. Kargar and M. M. Green, "A 10 Gb/s adaptive analog decision feedback equalizer for multimode fiber dispersion compensation in 0.13 μm CMOS," in *2010 Proc. of the ESSCIRC*, pp. 550–553 (2010).
31. S. Jain et al., "Multi-element fiber technology for space-division multiplexing applications," *Opt. Express* **22**(4), 3787–3796 (2014).
32. V. S. Lyubopytov, V. K. Bagmanov, and A. K. Sultanov, "Adaptive SLM-based compensation of intermodal interference in few-mode optical fibers," *Proc. SPIE* **9216**, 92160I (2014).
33. S. Randel et al., "6 × 56-Gb/s mode-division multiplexed transmission over 33-km few-mode fiber enabled by 6 × 6 MIMO equalization," *Opt. Express* **19**(17), 16697–16707 (2011).
34. A. Amphawan et al., "Real-time holographic backlighting positioning sensor for enhanced power coupling efficiency into selective launches in multimode fiber," *J. Mod. Opt.* **59**(20), 1745–1752 (2012).
35. A. Amphawan, "Binary encoded computer generated holograms for temporal phase shifting," *Opt. Exp.* **19**(23), 23085–23096 (2011).
36. I. Rsoft Design Group, "OptSim user guide," Optsim 5.2, Synopsis (2010).
37. *MATLAB, The MathWorks, Inc.*, Matlab R2016a, Mathworks Natick, Massachusetts.
38. P. V. Mena et al., "A comprehensive circuit-level model of vertical-cavity surface-emitting lasers," *J. Lightwave Technol.* **17**(2), 2612–2632 (1999).
39. J. W. Scott et al., "Modelling temperature effects and spatial hole burning to optimize vertical-cavity surface-emitting laser performance," *IEEE J. Quantum Electron.* **29**(5), 1295–1308 (1993).
40. J. Carpenter et al., "Mode multiplexing at 2 × 20 Gbps over 19-cell hollow-core photonic band gap fibre," in *2012 Optical Fiber Communication Conf. and Exposition and the National Fiber Optic Engineers Conf.* (2012).
41. A. W. Snyder and J. D. Love, *Optical Waveguide Theory*, Chapman and Hall, London (1983).
42. J. Gowar, *Optical Communication Systems*, 2nd ed., Prentice Hall, New York (1993).
43. R. Olshansky and S. M. Oaks, "Differential mode attenuation measurements in graded-index fibers," *Appl. Opt.* **17**(11), 1830–1835 (1978).
44. J. Yadlowsky and A. R. Mickelson, "Distributed loss and mode coupling and their effect on time-dependent propagation in multimode fibers," *Appl. Opt.* **32**(33), 6664–6677 (1993).
45. M. Abramowitz and I. A. Stegun, *Handbook of Mathematical Functions: With Formulas, Graphs and Mathematical Tables*, 9th Dover printing, with additional corr. ed., Dover Publications, New York (1973).
46. A. Amphawan and W. A. Alabdalleh, "Simulation of properties of the transverse modal electric field of an infinite parabolic multimode fiber," *Microwave Opt. Technol. Lett.* **54**(6), 1362–1365 (2012).
47. I. S. Gradshteyn and I. M. Ryzhik, *Tables of Integrals, Series and Products*, A. Jeffrey and D. Zwillinger, Eds., 7th ed., pp. xiv+1086, Elsevier (1965).
48. L. Geng et al., "Symmetrical 2-D Hermite–Gaussian square launch for high bit rate transmission in multimode fiber links," in *Optical Fiber Communication Conf. and Exposition (OFC/NFOEC), 2011 and the Nat. Fiber Optical Engineering Conf.*, pp. 1–3 (2011).

Angela Amphawan received her PhD in optical engineering from University of Oxford, UK. She leads the Optical Computing Research Laboratory at Universiti Utara Malaysia and is a Fulbright fellow at the Massachusetts Institute of Technology, Cambridge, USA. She has been invited as a keynote speaker for several Fulbright and IEEE conferences, and has won two best paper awards. She has served on the Editorial Board of Wiley Transactions on Emerging Telecommunications Technologies, International Journal of Electrical and Computer Engineering and several others. She has also served as publicity cochair for the IEEE Wireless Communications and Networking Conference (WCNC). She has over 100 referred publications and a patent.

Yousef Fazea obtained his Bachelor of information technology and Master of Science in information technology from Universiti Utara Malaysia in 2011 and 2012, respectively. He is currently a PhD candidate at the Optical Computing and Technology Research Laboratory at the School of Computing, Universiti Utara Malaysia.